Regional heart motion abnormality detection: An information theoretic approach

Kumaradevan Punithakumar [a,*], Ismail Ben Ayed [b], Ali Islam [c], Aashish Goela [d], Ian G. Ross [d], Jaron Chong [e], Shuo Li [b]

[a] Servier Virtual Cardiac Centre, Department of Radiology & Diagnostic Imaging, University of Alberta, Edmonton, AB, Canada
[b] GE Healthcare, London, ON, Canada
[c] St. Joseph's Health Care, London, ON, Canada
[d] London Health Sciences Centre, London, ON, Canada
[e] Department of Diagnostic Radiology, McGill University, Montreal, QC, Canada

ABSTRACT

Tracking regional heart motion and detecting the corresponding abnormalities play an essential role in the diagnosis of cardiovascular diseases. Based on functional images, which are subject to noise and segmentation/registration inaccuracies, regional heart motion analysis is acknowledged as a difficult problem and, therefore, incorporation of prior knowledge is desirable to enhance accuracy. Given noisy data and a nonlinear dynamic model to describe myocardial motion, an unscented Kalman smoother is proposed in this study to estimate the myocardial points. Due to the similarity between the statistical information of normal and abnormal heart motions, detecting and classifying abnormality is a challenging problem. We use the Shannon's differential entropy of the distributions of potential classifier features to detect and locate regional heart motion abnormality. A naive Bayes classifier algorithm is constructed from the Shannon's differential entropy of different features to automatically detect abnormal functional regions of the myocardium. Using 174 segmented short-axis magnetic resonance cines obtained from 58 subjects (21 normal and 37 abnormal), the proposed method is quantitatively evaluated by comparison with ground truth classifications by radiologists over 928 myocardial segments. The proposed method performed significantly better than other recent methods, and yielded an accuracy of 86.5% (base), 89.4% (mid-cavity) and 84.5% (apex). The overall classification accuracy was 87.1%. Furthermore, standard kappa statistic comparisons between the proposed method and visual wall motion scoring by radiologists showed that the proposed algorithm can yield a kappa measure of 0.73.

© 2012 Elsevier B.V. All rights reserved.

1. Introduction

Assessment of left ventricular (LV) function is of utmost importance in the diagnosis of coronary heart disease, the leading cause of death worldwide. The LV function can be assessed in part using *global* indicators such as ejection fraction, stroke volume or ventricular mass. Providing only an overall appraisal of the LV function, such global indicators lack information about localized ventricular function. Therefore, *regional wall motion abnormality* analysis is preferred for a thorough clinical analysis. In clinical practice, regional wall motion is commonly scored following a standard issued by the American Heart Association (Cerqueira et al., 2002), which suggests selecting representative 2D cardiac slices to generate 17 standardized LV segments. Such analysis relies on visual assessments and interpretations of the motions of each of the 17 segments and, therefore, is subject to high interobserver variability (Hoffmann et al., 2006; Redheuil et al., 2007),

subjective and nonreproducible. The difficulties come from the subtle visual differences between normal- and abnormal-segment motions. For example, the clinical study by Hoffmann et al. (2006) shows that the mean kappa measure of detecting regional wall motion abnormalities by three different radiologists could be as low as 0.43. Alternatively, automating abnormality scoring attracted a significant research effort in recent years.

Earlier studies of wall motion abnormality detection used echocardiography (Bosch et al., 2005; Leung et al., 2007; Mansor and Noble, 2008), with focus on techniques such as shape statistics (Bosch et al., 2005; Leung et al., 2007) and hidden Markov models (Mansor and Noble, 2008), among others. More recently, MRI-based wall motion abnormality detection attracted a significant research attention (Qian et al., 2008; Lu et al., 2009; Suinesiaputra et al., 2009; Garcia-Barnes et al., 2010; Lekadir et al., 2011). The work in (Lu et al., 2009) suggested normalizing the LV to the same position, size and intensity level, and used a correlation-based intra-segment classification to discriminate normal and abnormal motions. This preliminary study was evaluated only on basal slices. The study in (Suinesiaputra et al., 2009) used an independent

* Corresponding author.
E-mail address: punithak@ualberta.ca (K. Punithakumar).

Nomenclature

AUC	area under the receiver operating characteristic curves	ROC	receiver operating characteristic
DENSE	displacement encoding with stimulated echoes	SDE	Shannon's differential entropy
FIESTA	fast imaging employing steady state acquisition	UKF	unscented Kalman filter
LV	left ventricle	UKS	unscented Kalman smoother
MR	magnetic resonance		

component analysis classifier to detect and localize abnormally contracting regions. The authors of (Lekadir et al., 2011) focused on statistical modeling based on spatiotemporal interlandmark relationships. The study in (Garcia-Barnes et al., 2010) used a differentiable manifold based analysis. Most of the existing algorithms are built on statistical shape analysis techniques (Suinesiaputra et al., 2009; Lekadir et al., 2011) which may require large training sets, with the results highly dependent on the choice of the training data and, therefore, often biased towards a particular cardiac pathology. Moreover, in some cases, the existing algorithms either use data that are not frequently available in regular clinical routine (Garcia-Barnes et al., 2010; Qian et al., 2008), or require extensive user interactions to define manually myocardial boundaries in the training phase (Suinesiaputra et al., 2009; Lekadir et al., 2011). For instance, the studies in (Garcia-Barnes

et al., 2010; Qian et al., 2008) used tagged MR images, which allow extracting additional features, e.g., myocardial strain. However, in clinical routine, most patients are scanned for cine MR, and only a few of them have tagged MR images. Despite this impressive research effort that has been recently devoted to automatic detection and localization of regional abnormality, the problem is still acknowledged challenging, with a large room for improvements in regard to accuracy. For instance, a recent publication (Suinesiaputra et al., 2009) reports an accuracy of 63.70% (base), 67.41% (middle), and 66.67% (apex) when visual wall motion scoring is used as reference.

Our goal is to develop an automated tool to detect and localize myocardial segments that show abnormal contractile behavior using standard clinical magnetic resonance (MR) images, and to do so with limited user interaction. Fig. 11 shows an example of
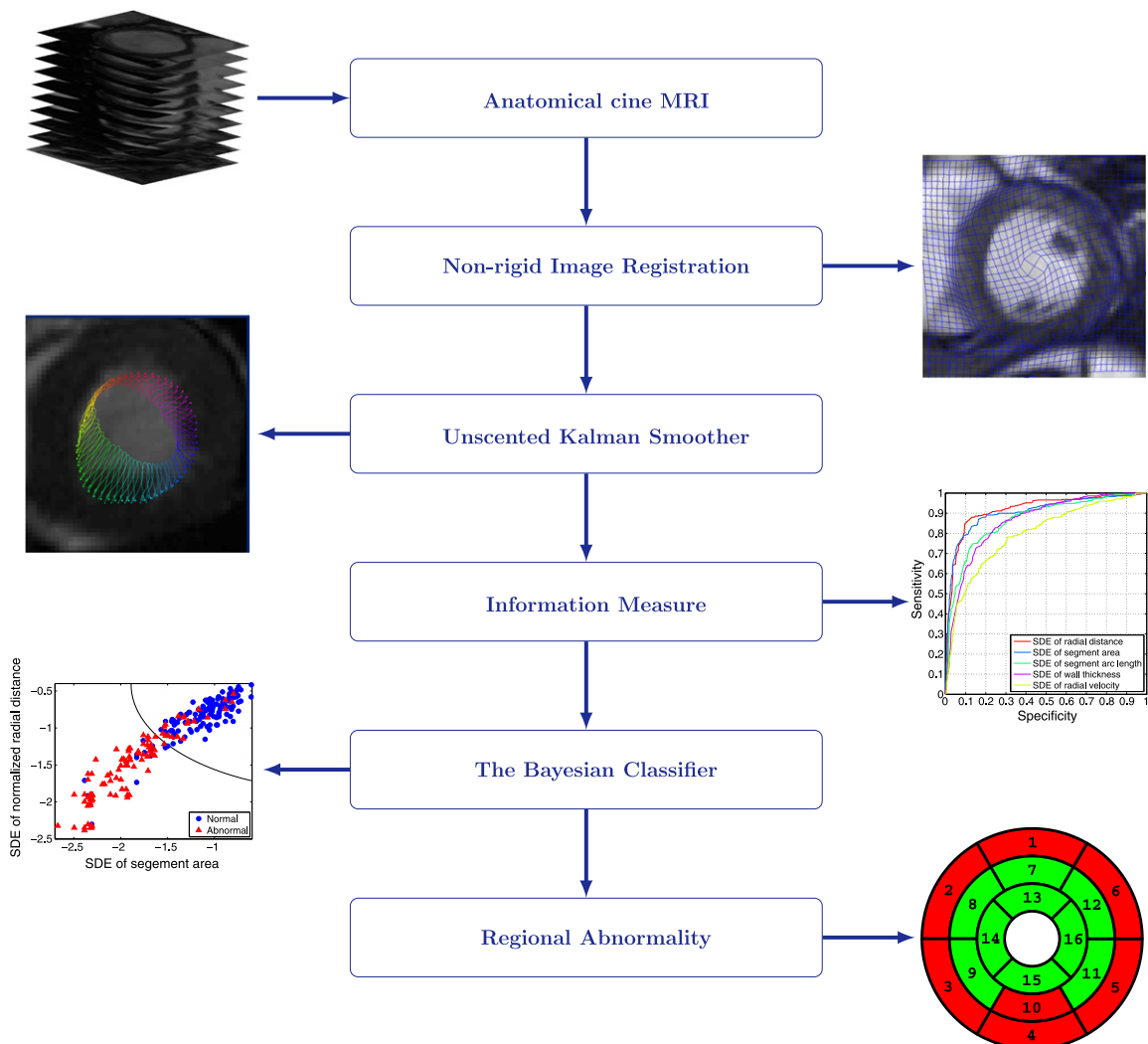

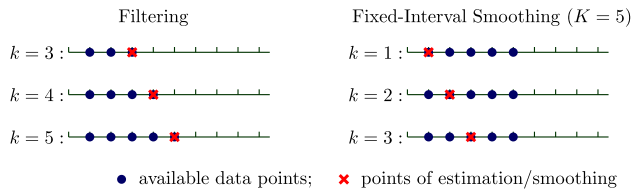Fig. 1. The proposed regional heart abnormality detection algorithm.

Fig. 2. An example comparison between filtering and fixed-interval smoothing. In filtering, the estimation is based only on past observations, whereas in fixed-interval smoothing, these estimates can be improved using observations received afterwards.
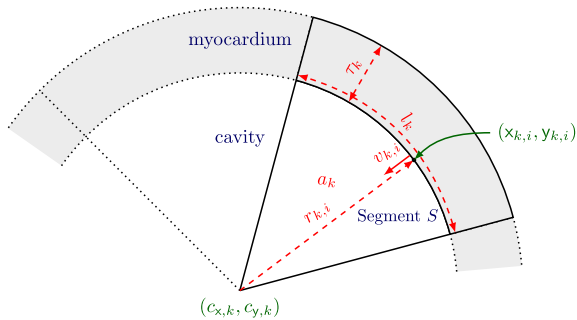

Fig. 3. Classifier features corresponding to segment S at frame k. The following features were used in our analysis: normalized radial distance $r_{k,i}$, radial velocity $v_{k,i}$, segment arc length l_k, segment area a_k and wall thickness τ_k.
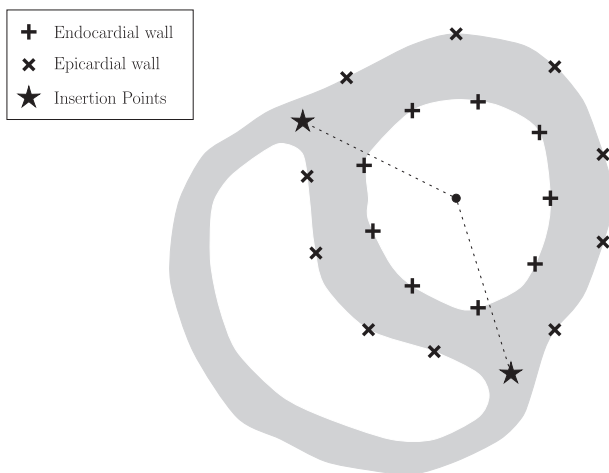

Fig. 4. User input to specify initial segmentation and anatomical landmarks on the first frame. In subsequent frames, anatomical landmarks are obtained automatically using the registration method (Chen et al., 2010).

binary score results, *i.e.*, normal or abnormal contractility, for the segments of a myocardium. The proposed abnormality detection system primarily consists of preprocessing and classification.

1.1. Preprocessing

The main objective of this preprocessing step is to estimate regional wall motion quantitatively. Many of the existing motion tracking techniques rely on myocardial tagging (Arts et al., 2010; Liu and Prince, 2010; Young, 1999) or other MR acquisition protocols that provide velocity information such as phase-contrast velocity or displacement encoding with stimulated echoes (DENSE) (Bergvall et al., 2008; Gilliam et al., 2009; Pan et al., 2005; Spottiswoode et al., 2007). Unfortunately, these MR acquisition protocols

are still limited in routine clinical use due to their complex and time-consuming post-processing and interpretation. Anatomical cine MR is recognized as the reference MR standard to assess regional and global cardiac function. One can still use manual delineation of the myocardium on anatomical cine MR images, and subsequently estimate the myocardial wall motion. However, cine MR provides a large number of images[1] and, therefore, tracking based on manual delineation of the LV boundary in all these images is prohibitively time consuming. Therefore, automating the process can be of great interest (Petitjean and Dacher, 2011). Automatic delineation of myocardium is difficult because of the low contrast and photometric similarities between the connected cardiac regions – for instance, the papillary muscles within the cavity and myocardial wall have approximately the same intensity. Further, the substantial variations in size, shape and intensity between subjects, particularly those with pathological patterns, makes geometric/photometric models hard to build from a finite training set. To tackle the problem of delineation of the myocardium, we propose to use a nonrigid registration method developed recently (Chen et al., 2010), given anatomical landmarks on the first frame. Using registration is advantageous in our study as it provides the sequence of corresponding points over time, an essential attribute to analyze wall motion regionally. In contrast, using a segmentation algorithm, e.g., (Ben Ayed et al., 2008; Ben Ayed et al., 2009), would further require additional computations to obtain the point-to-point correspondences.

We can estimate the motion of the myocardial points quantitatively using the point-to-point correspondence obtained from the registration algorithm. However, accurate characterization of the dynamic behavior of the LV is essential in order to enhance the performance of motion estimation. Such temporal characteristic of LV motion can be incorporated by having a dynamic state-space model (Jacob et al., 2001; Liu and Shi, 2007; Moireau et al., 2009; Punithakumar et al., 2010b). (Jacob et al., 2001) used a second-order autoregressive model to describe the endocardial motion. This approach generally requires a training to determine coefficient matrices of the autoregressive model. (Liu and Shi, 2007) used a constant-velocity (linear) model, a well known state-space model for target tracking applications. This model is designed for objects moving on a straight line and, therefore, may not yield an accurate characterization of cardiac motion.

In this study, we propose a cyclic dynamic model that is more descriptive of the periodic motion of the myocardium than the model with a fixed angular frequency in (Punithakumar et al., 2010c). The model in (Punithakumar et al., 2010c) is insufficient to describe the LV dynamics because: (1) The angular frequency that characterizes the cyclic motion of an LV point for normal subjects changes over time; (2) the dynamics of LV motion in systolic and diastolic phases are significantly different; (3) the LV dynamics of abnormal subjects differ significantly from those of normal subjects. One approach to address the aforementioned problems is to use a multiple-model description with different angular frequencies to characterize different modes of the LV dynamics (Punithakumar et al., 2010b). However, such an approach requires multiple filters running in parallel and, therefore, more computational resources.

The model that we propose in this study embeds a time-varying angular frequency that has to be estimated from the data along with other state elements. Based on a more general description of cyclic motion, a time-varying angular frequency would allow to describe more accurately different phases of the cardiac cycle. However, this is not straightforward because embedding time-varying angular frequency within a cyclic dynamic model yields

---

[1] Typically, the number of images per subject is equal to 200.

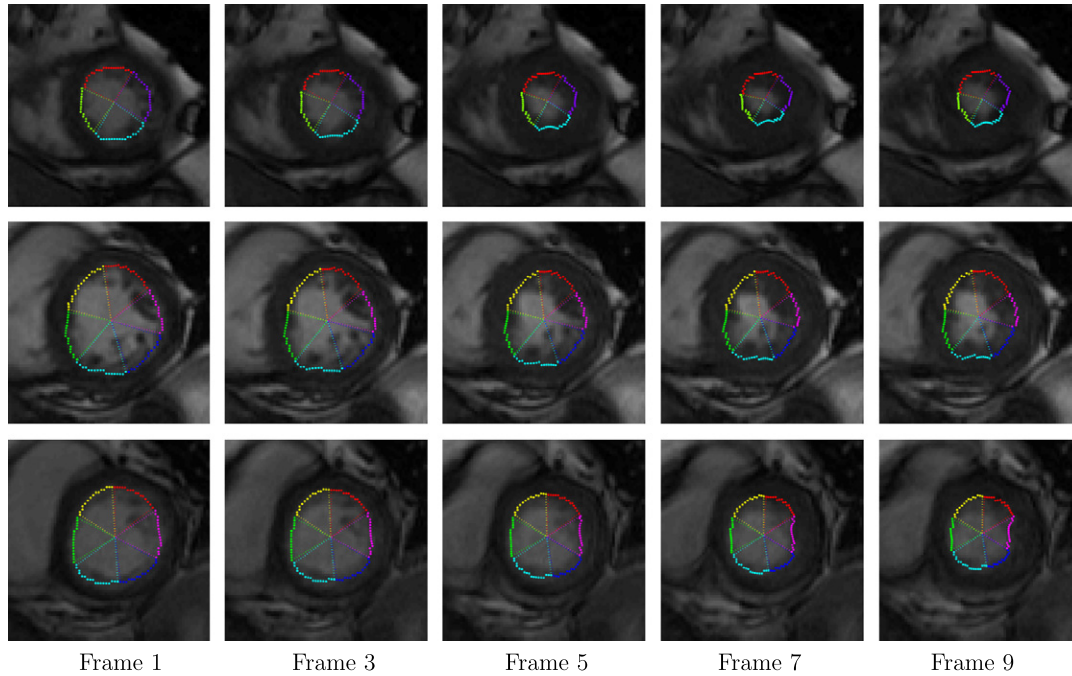| Frame 1 | Frame 3 | Frame 5 | Frame 7 | Frame 9 |

Fig. 5. Representative examples of segmented endocardium using the proposed approach. Apical (first row), mid-cavity (second row) and basal (third row) frames were segmented, respectively, into 4, 6 and 6 segments following the standard in Cerqueira et al. (2002). In the first frame, a cubic spline interpolation was used to obtain more sample points along the endocardial boundary using a similar user input as in Fig. 4. These sample points were propagated in subsequent frames using a nonrigid registration and UKS.
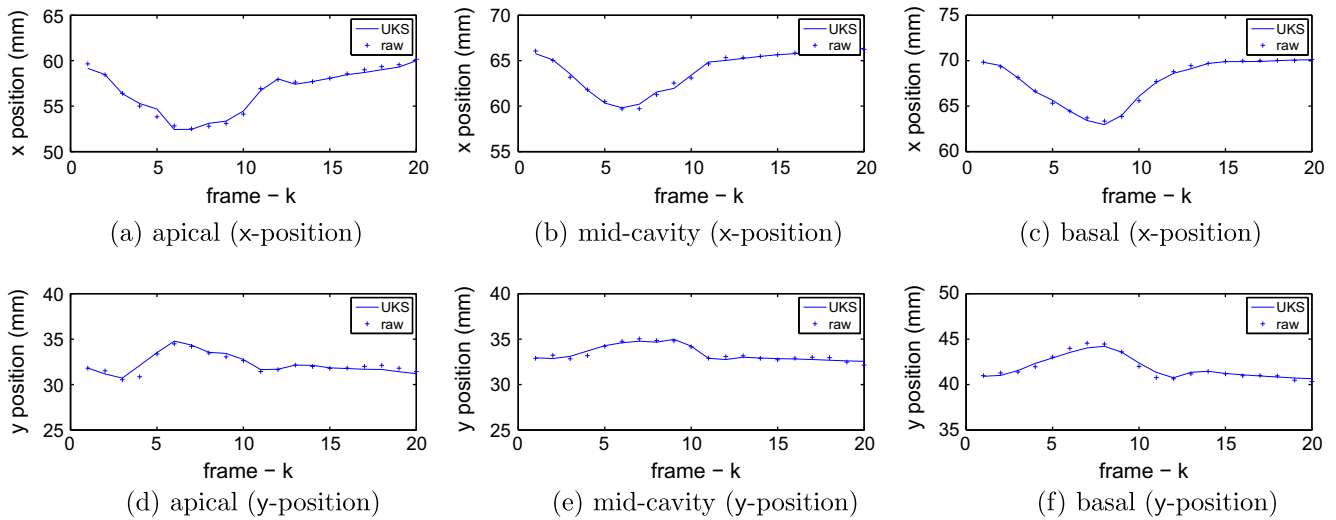

(a) apical (x-position)   (b) mid-cavity (x-position)   (c) basal (x-position)

(d) apical (y-position)   (e) mid-cavity (y-position)   (f) basal (y-position)

Fig. 6. Raw values from nonrigid registration and the subsequent UKS estimates for three representative sample points respectively on apical (1st column), mid-cavity (2nd column) and basal frames (3rd column).

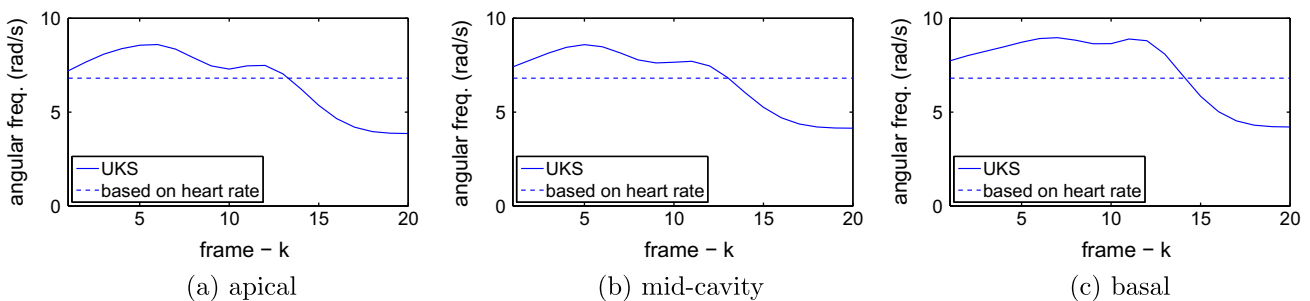(a) apical   (b) mid-cavity   (c) basal

Fig. 7. Estimation of angular frequency ω_k using UKS for three representative sample points on apical, mid-cavity and basal frames. The dotted lines show the value calculated using the heart rate, $2\pi/(K\Delta T)$. The ω_k value estimates are higher at the beginning of the cardiac cycle (systolic phase), and lower at the end (diastolic phase).
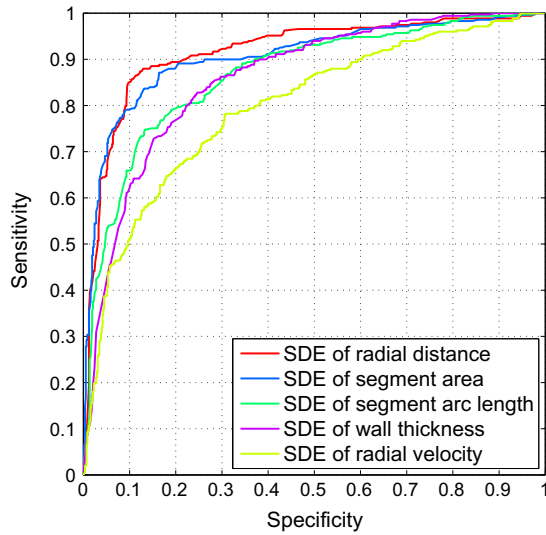
Fig. 8. Receiver operating characteristics of classifier features. The closer the curve to the left hand top corner, the better the classification performance.

and covariance information, which addresses the deficiencies of linearization inherent to other adaptive filters such as the extended Kalman filter. UKF propagates the second order properties of the distribution with only a small amount of statistical information by choosing sample points deterministically. Therefore, it provides sufficient accuracy for nonlinear filtering applications with a computational cost of an order similar to the extended Kalman filter.

1.2. Classification

The classification part is a difficult problem due to the similarities associated with the normal and abnormal heart motions (Fung et al., 2005; Qazi et al., 2007; Punithakumar et al., 2010c). In this study, we use the Shannon's differential entropy (SDE) of the distributions of *normalized radial distance, radial velocity, segment area (endocardial), segment arc length (endocardial) and wall thickness* for regional wall motion abnormality detection. Rather than relying on elementary measurements or a fixed set of moments, the SDE measures the whole distribution information. In the context of *global (not local) classification* of normal and abnormal hearts, the SDE has been shown to be more discriminative than commonly used descriptors (Punithakumar et al., 2010c). In this study, we investigate the SDE in the context of the more challenging and complex task of regional classification.

The individual classification ability of features were measured using receiver operating characteristic (ROC) curves with the corresponding area under the curves (AUCs), and the Bhattacharyya distance metric (Comaniciu et al., 2003). Subsequently, a naive Bayes classifier algorithm (Seber, 1984) is constructed from the SDEs of classifier features with the best performance in order to automatically detect abnormal functional regions of the myocardium.

a *nonlinear* estimation problem, which cannot be accurately solved with the classical Kalman filter. The most common solution would be to use an extended Kalman filter based on linearized approximations, but such solution is known to yield extremely poor results in practice (Julier and Uhlmann, 2004).

To address the aforementioned difficulties, we propose an unscented Kalman smoother (UKS), a smoothing algorithm developed based on the Unscented Kalman filter (UKF) (Julier and Uhlmann, 2004), for state estimation. The UKF uses unscented transformation, a more direct and explicit mechanism for transforming mean

(a) SDE of radial distance
$\mathcal{B} = 0.60$

(b) SDE of segment area
$\mathcal{B} = 0.59$

(c) SDE of wall thickness
$\mathcal{B} = 0.49$

(d) SDE of segment arc length
$\mathcal{B} = 0.48$

(e) SDE of radial velocity
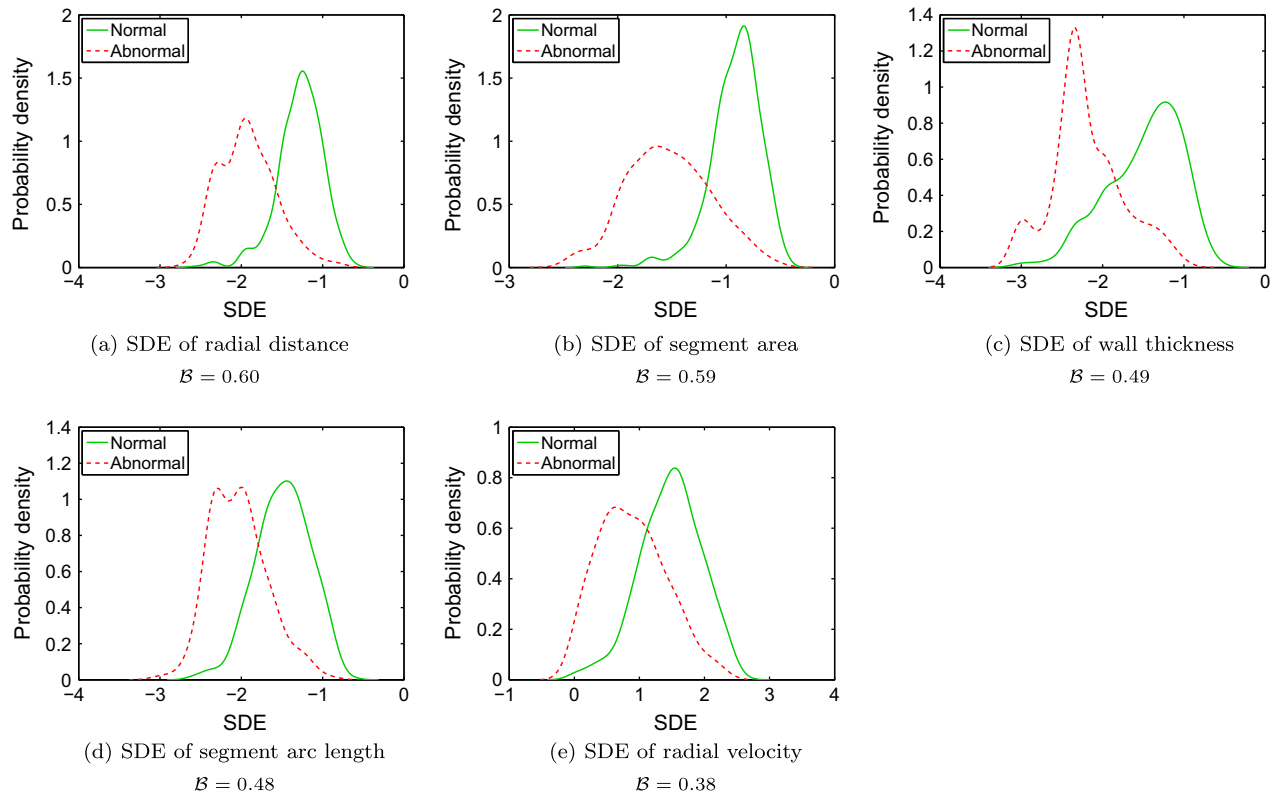$\mathcal{B} = 0.38$

Fig. 9. Distributions of normal and abnormal segments with corresponding Bhattacharyya distance metric $\mathcal{B}$, categorized using different classifier features over 928 myocardial segments.
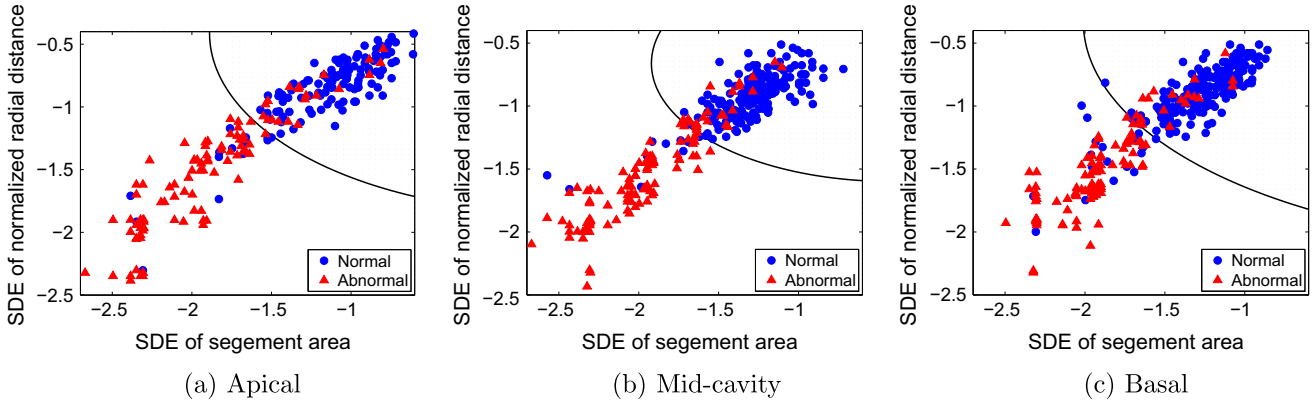
Fig. 10. Decision boundary for normal and abnormal regional myocardial functions constructed using a Bayesian classifier. The boundary was constructed separately for each apical, mid-cavity and basal frames using a dataset of 58 subjects.
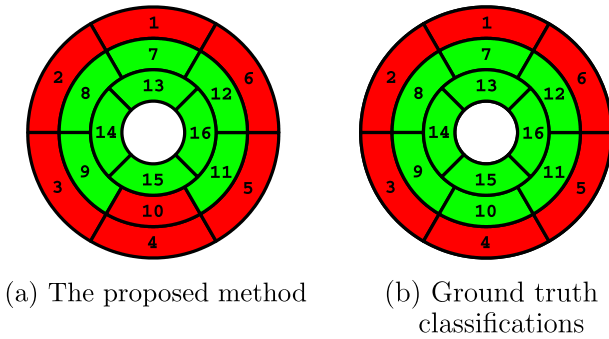

Fig. 11. Representative example of classification results of myocardial segments following the standard issued by American Heart Association (Cerqueira et al., 2002). The circumferential polar plots depict the results by the proposed method and ground truth classifications by radiologist of 16 myocardial segments: 1. basal anterior 2. basal anteroseptal 3. basal inferoseptal 4. basal inferior 5. basal inferolateral 6. basal anterolateral 7. mid anterior 8. mid anteroseptal 9. mid inferoseptal 10. mid inferior 11. mid inferolateral 12. mid anterolateral 13. apical anterior 14. apical septal 15. apical inferior 16. apical lateral. The 17th segment, apex, is not analyzed. Normal and abnormal motions are shown, respectively, by green and red colors. Comparisons with ground truth classifications show that 15 out of 16 segments were correctly classified by the proposed method. (For interpretation of the references to colour in this figure legend, the reader is referred to the web version of this article.)

1.3. Contributions of this paper

We can summarize the contributions of the current study as follows:

- We propose to use a nonrigid registration algorithm (Chen et al., 2010) to obtain a sequence of corresponding points over time, given an initial set of points on the first frame.
- We propose a nonlinear state transition model constructed by adding a time-varying angular frequency to the state-space model in (Punithakumar et al., 2010c).
- We propose to use a naive Bayes classifier constructed from the area and radial motion metrics.

Using 174 segmented short-axis magnetic resonance cines obtained from 58 subjects (21 normal and 37 abnormal), the proposed method is quantitatively evaluated by comparison with ground truth classifications by radiologists over 928 myocardial segments. The proposed method performed significantly better than other recent methods, and yielded an accuracy of 86.5% (base), 89.4% (mid-cavity) and 84.5% (apex). The overall classification accuracy was 87.1%. Furthermore, standard kappa statistic

comparisons between the proposed method and visual wall motion scoring by radiologists showed that the proposed algorithm can yield a kappa measure of 0.73.

A preliminary conference version of this work appeared in MICCAI 2010 (Punithakumar et al., 2010a). This journal version expands on (Punithakumar et al., 2010a) with (1) a wider experimental investigation that includes more patient data, radiologist assessments, and statistical validations; and (2) a much broader, more informative/rigorous discussion of the subject.

2. Methods

Fig. 1 gives the components of the overall abnormality detection algorithm. In this section, we describe the functionality of each individual component.

2.1. Data preprocessing using nonrigid image registration

In order to obtain a sequence of points over time, we formulate the point correspondence between the first image T_1 and kth image T_k defined over $\Omega \subset \mathbb{R}^2$ as the optimization of similarity/dissimilarity measure (Chen et al., 2010).

$$\hat{\phi} = \arg\underset{\phi}{\mathrm{opt}}\ E_s(T_1, T_k, \phi(\xi)) \tag{1}$$

for each pixel location $\xi \in \Omega$, where $\phi: \Omega \to \Omega$ is a transformation function, and $E_s(\cdot)$ a measure of similarity. This problem may not have a unique solution. Therefore, a deformation field is introduced with Jacobian transformation μ and curl of end velocity field γ, where $\mu: \Omega \to \mathbb{R}$ and $\gamma: \Omega \to \mathbb{R}$ (these will be described in more details later).

2.1.1. Moving mesh generation

Let $\mu(\xi)$ be a continuous monitor function constrained by

$$\int_\Omega \mu = |\Omega| \tag{2}$$

The purpose of this step is to find a transformation $\phi: \Omega \to \Omega$, $\partial\Omega \to \partial\Omega$, so that

$$J_\phi(\xi) = \mu(\xi) \tag{3}$$

where J_ϕ denotes the transformation Jacobian. The following computations yield a transformation ϕ which verifies (3).

Step 1: Compute a vector field $\rho(\xi)$ which verifies

$$\mathrm{div}\ \rho(\xi) = \mu(\xi) - 1 \tag{4}$$

Step 2: Build a velocity vector field from $\rho(\xi)$:

$$v_t(\xi) = \frac{\rho(\xi)}{t + (1-t)\mu(\xi)}, \qquad t \in [0,1] \tag{5}$$

where t is an artificially introduced (algorithmic) time.

Step 3: Finally, ϕ is obtained by solving the following ODE:

$$\frac{d\psi(\xi,t)}{dt} = v_t(\psi(\xi,t)), \qquad t \in [0,1], \ \psi(\xi,t=0)=\xi \tag{6}$$

and setting ϕ equal to ψ evaluated at $t = 1$: $\phi(\xi) = \psi(\xi, t = 1)$.

The above problem does not have a unique solution. However, a unique solution can be obtained by adding to (4) an additional constraint on the curl of $\rho(\xi)$, and solving the ensuing div-curl system under the Dirichlet boundary condition:

$$\text{div } \rho(\xi) = \mu(\xi) - 1 \tag{7a}$$
$$\text{curl } \rho(\xi) = \gamma(\xi) \tag{7b}$$

with null boundary condition $\rho(\xi) = 0 \forall \xi \in \partial\Omega$, where $\gamma(\xi)$ is a continuous function over Ω. Hence, the transformation can be fully parameterized by $J_\phi(\xi)$ and $\gamma(\xi)$. Note that the Dirichlet boundary conditions are required to ensure the uniqueness of the solution (Zhou, 2006). The Dirichlet boundary conditions may cause the motion errors to be high at the image boundaries. However, this can be easily overcome by padding both images by zeros.

With the above parameterization, (1) can be reformulated as the following constrained optimization problem (Chen et al., 2010):

Problem 1. Given two images T_1 and T_k, defined over Ω, find the function pair $\{\mu(\xi), \gamma(\xi)\}$, that optimizes the cost in (1), subject to:

$$\int_\Omega \mu(\xi) d\xi = |\Omega| \tag{8a}$$
$$\tau_h > \mu(\xi) > \tau_l, \quad \xi \in \Omega' \subset \Omega \tag{8b}$$

where $0 < \tau_l$ ensuring that $\phi_{\mu,\gamma}$ is a diffeomorphism, and Ω' is a subregion of image domain Ω.

Constraint (8a) ensures the areas of the domain and co-domain are equal after transformation, whereas (8b) enforces the *incompressibility* constraint in sub-region Ω'. Note that a diffeomorphism corresponds to a positive transformation Jacobian. We enforce such a positiveness explicitly via the monitor function (Liu, 2006).

The above problem is solved by a *step-then-correct* optimization strategy as described in Algorithm 1. We refer the reader to (Chen et al., 2010) for derivation and numerical implementation details.

Algorithm 1. Step-then-correct optimization (Chen et al., 2010)

Given image pair T_1 and T_k, consider the following steps.

Step 1 Compute the gradients of μ and γ which we denote respectively by $\nabla\mu(T_1, T_k, \phi)$ and $\nabla\gamma(T_1, T_k, \phi)$

Step 2 Terminate if step size $\delta < \delta_{th}$ or a maximum number of iterations is reached; otherwise, update (μ, γ) by (i is the iteration number):

$$\mu^{i+1} = \mu^i + \delta \frac{\nabla\mu E_S}{\max|\nabla\mu E_S|} \quad \text{and} \quad \gamma^{i+1}$$
$$= \gamma^i + \delta \frac{\nabla\gamma E_S}{\max|\nabla\gamma E_S|}$$

Step 3 For each pixel location $\xi \in \Omega' \subset \Omega$, impose constraint (8b) by

$$\mu^{i+1}(\xi) \leftarrow \max(\mu^{i+1}(\xi), \tau_l) \quad \text{and} \quad \mu^{i+1}(\xi)$$
$$\leftarrow \min(\mu^{i+1}(\xi), \tau_h)$$

For each pixel location $\xi \in \Omega$, impose constraint (8a) by

$$\mu^{i+1}(\xi) \leftarrow \mu^{i+1}(\xi) \frac{|\Omega|}{\sum_{\xi \in \Omega} \mu^{i+1}(\xi)}$$

Step 4 Find a vector field $\rho(\xi)$ which satisfies:

$$\text{div } \rho(\xi) = \mu^{i+1}(\xi) - 1 \tag{9a}$$
$$\text{curl } \rho(\xi) = \gamma^{i+1}(\xi) \tag{9b}$$

with null boundary condition $\rho(\xi) = 0$, $\forall \xi \in \partial\Omega$. Compute the transformation $\phi(\xi) = \psi(\xi, t = 1)$ by finding the solution to the ordinary differential equation

$$\frac{d\psi(\xi,t)}{dt} = v_t(\psi(\xi,t)) \qquad t \in [0,1] \tag{10}$$

with $\psi(\xi, t = 0) = \xi$. The velocity vector field v_t is given by

$$v_t(\xi) = \frac{\rho(\xi)}{t + (1-t)\mu^{i+1}(\xi)} \quad t \in [0,1] \tag{11}$$

Step 5 Compute cost E_S. If it improves, $i \leftarrow i + 1$, go to Step 1; otherwise, decrease δ and go to Step 2.

2.2. Constructing information theoretic measures for classification

2.2.1. Dynamic model for temporal periodicity

Let (x, y) be the Cartesian coordinates of a point on the myocardium with the origin corresponding to the lower left corner of the image. Consider the state vector $\zeta = [\bar{x} \times \dot{x}]^T$ that describes the dynamics of the point in x-coordinate direction, where $\dot{x}$ and $\bar{x}$ denote, respectively, velocity and the mean position over cardiac cycle. We assume the heart motion is periodic. Then, we define a *continuous state-space* model that describes the cyclic motion of the point as follows:

$$\dot{\zeta}(t) = \begin{bmatrix} 0 & 0 & 0 \\ 0 & 0 & 1 \\ \omega^2 & -\omega^2 & 0 \end{bmatrix} \zeta(t) + \begin{bmatrix} 1 & 0 \\ 0 & 0 \\ 0 & 1 \end{bmatrix} w(t) \tag{12}$$

where ω is the angular frequency, and $w(t)$ a vector-valued white noise. For a constant value of ω and $w(t) = 0$, model (12) amounts to a simple harmonic oscillation in x-direction. However, cardiac motion is much more complex than a single harmonic motion and, therefore, we propose to embed (1) a time-varying ω so as to account for the rate of oscillation change and (2) a new variable $w(t)$ for unpredictable errors. We derive the *discrete-time equivalent* of (12) as follows (refer to Appendix A for derivation details):

$$\zeta_{k+1} = F_k \zeta_k + w_k \tag{13}$$

where k is the frame number (or time step), and F_k given by:

$$F_k = \begin{bmatrix} 1 & 0 & 0 \\ 1 - \cos(\omega_k \Delta T) & \cos(\omega_k \Delta T) & \frac{1}{\omega_k}\sin(\omega_k \Delta T) \\ \omega_k \sin(\omega_k \Delta T) & -\omega_k \sin(\omega_k \Delta T) & \cos(\omega_k \Delta T) \end{bmatrix} \tag{14}$$

w_k is a discrete-time white noise sequence, ΔT the sampling interval, and ω_k a discrete angular frequency. The covariance of process noise $Q_k = \text{cov}(w_k)$ is given by

$$Q_k = [q_{ij}]_{3 \times 3} \tag{15}$$

where q_{ij}'s are defined in (A.21)–(A.26) in Appendix A.

Let $\mathbf{s}_k = [\bar{x}_k \ x_k \ \dot{x}_k \ \bar{y}_k \ y_k \ \dot{y}_k \ \omega_k]^T$ be the state vector that describes the corresponding dynamics at time step k. Elements $\dot{x}_k$, $\bar{x}_k$, $\dot{y}_k$ and $\bar{y}_k$ denote, respectively, the velocity and mean position over a cardiac cycle in $\times$ and y coordinate directions. We compute a sequence of corresponding points in all the frames using transformation function $\hat{\phi}$ (Eq. (1)).

The discrete-time dynamic model that describes the cyclic motion of the point is given by:

$$\mathbf{s}_{k+1} = f_k(\mathbf{s}_k) + v_k \tag{16}$$

where

$$f_k(\mathbf{s}_k) = \begin{bmatrix} F_k & \mathbf{0}_{3\times3} & \mathbf{0}_{3\times1} \\ \mathbf{0}_{3\times3} & F_k & \mathbf{0}_{3\times1} \\ \mathbf{0}_{1\times3} & \mathbf{0}_{1\times3} & 1 \end{bmatrix} \tag{17}$$

and $\{v_k\}$ denotes a Gaussian process noise sequence that accommodates unpredictable errors due to modeling uncertainties, with zero-mean and covariance given by blkdiag (Q_k, Q_k, q_3), where blkdiag $(\cdot)$ denotes block diagonal matrix (refer to Appendix A for further details on the expressions and meanings of Q_k and q_3).

The measurement equation is given by

$$z_k = H_k\mathbf{s}_k + \eta_k \tag{18}$$

where

$$H_k = \begin{bmatrix} 0 & 1 & 0 & 0 & 0 & 0 & 0 \\ 0 & 0 & 0 & 0 & 1 & 0 & 0 \end{bmatrix} \tag{19}$$

$\{\eta_k\}$ is a zero-mean Gaussian noise sequence with covariance

$$R_k = \begin{bmatrix} r & 0 \\ 0 & r \end{bmatrix} \tag{20}$$

We use parameter r to characterize the uncertainties associated with the observations due to error. The measurement errors in our study are mainly due to displacement inaccuracies arising from nonlinear image registration as well as to the MR imaging noise. On the one hand, smaller values of r enforces the conformity of the estimation to the measurements, in which case erroneous measurements may result in low estimation accuracy. On the other hand, larger values of r may cause the measurements to be unreliable for the filter. The observation $z_k = [z_{k,x} \ z_{k,y}]^T$ corresponding to the point (x, y) is obtained using the displacement vectors from the registration method.

2.2.2. The recursive Bayesian filtering

Our objective is to build a Bayesian estimation of the dynamics of the LV, given model (12). Accurately estimating the state of such model is extremely difficult. The optimal Bayesian solution to the problem requires the propagation of the description of the full probability density function of the state $\mathbf{s}_k$. Because of the form of the density function is not restricted, we may not be able to describe it using a finite number of parameters, which requires approximations in practice. The Kalman filter, which is the most widely used estimation algorithm, uses only the mean and covariance information of the density function in its update rule. The extended Kalman filter is the most common extension to nonlinear systems; it uses a linearization of all nonlinear transformations. Unfortunately, such linearized transformations are not always reliable, and often result in inaccurate estimations when the error propagations cannot be approximated by a linear function. In this study, we adopt a recursive nonlinear Bayesian algorithm, the UKS, to estimate the state s_k at each time step. The UKS is a smoothing algorithm developed based on the UKF (Julier and Uhlmann, 2004). The UKF uses unscented transformation, a more direct and explicit mechanism for transforming mean and covariance information, that addresses the deficiencies of linearization inherent to other

adaptive filters. It propagates the second order properties of the distribution with only a small amount of statistical information by choosing sample points deterministically. Therefore, it provides sufficient accuracy for nonlinear filtering applications with a computational cost of an order similar to the extended Kalman filter.

To estimate the state X_k, the UKF uses only the set of observations $z_{1:k}$ from time step 1 to k. However, since the data in cardiac MRI is available upfront, the performance of the filtering algorithm can be further improved by smoothing (Sarkka, 2008) the estimation of the state X_k using observations $Z_{k:K}$, $K > k$, where K is the number of frames in an image sequence. There are several variants of smoothing, the most common being fixed-interval smoothing, which we use here. Fig. 2 depicts a comparison between the filtering approach and fixed-interval smoothing. Appendix B describes the details of the UKS.

2.3. Filter initialization

In our problem, we do not have prior knowledge of the initial value of $\mathbf{s}_1$. Therefore, we use two-point differencing method (Bar-Shalom et al., 2002) to initialize position and velocity components of the state. For instance, the initial position $\hat{x}_1$ and velocity $\hat{\dot{x}}_1$ in x-coordinate direction are given by

$$\hat{x}_1 = z_{1,x} \tag{21}$$

$$\hat{\dot{x}}_1 = \frac{(z_{2,x} - z_{1,x})}{\Delta T} \tag{22}$$

where $\{z_{k,x}: k = 1, 2, \ldots, K\}$ is the observation in x-coordinate direction obtained from kth frame. The mean position over cardiac cycle $\hat{\bar{x}}_1$ is initialized by taking the expectation over all corresponding measurements

$$\hat{\bar{x}}_1 = \frac{1}{K}\sum_{k=1}^{K} z_{k,x} \tag{23}$$

The initial state elements in y-coordinate direction, $\hat{y}_1$, $\hat{\dot{y}}_1$ and $\hat{\bar{y}}_1$, can be computed similarly using $\{z_{k,y}\}$. The angular velocity is initialized as $\omega_1 = 2\pi/(K\Delta T)$, and the initial mean input as $m_1 = [\hat{x}_1 \ \hat{\dot{x}}_1 \ \hat{\bar{x}}_1 \ \hat{y}_1 \ \hat{\dot{y}}_1 \ \hat{\bar{y}}_1 \ \omega_1]^T$. The corresponding covariance is given by

$$P_1 = \begin{bmatrix} \Phi_1 & \mathbf{0}_{3\times3} & \mathbf{0}_{3\times1} \\ \mathbf{0}_{3\times3} & \Phi_1 & \mathbf{0}_{3\times1} \\ \mathbf{0}_{1\times3} & \mathbf{0}_{1\times3} & 1 \end{bmatrix} \tag{24}$$

where

$$\Phi_1 = \begin{bmatrix} r & \frac{r}{K} & \frac{r}{K\Delta T} \\ \frac{r}{K} & r & \frac{r}{\Delta T} \\ \frac{r}{K\Delta T} & \frac{r}{\Delta T} & \frac{2r}{\Delta T^2} \end{bmatrix} \tag{25}$$

2.4. Information theoretic measures and classifier

The state estimates from UKS are subsequently processed towards the classification of normal or abnormal motions. In order to measure the information associated with regional LV function, the SDEs of a set of classifier features were evaluated. The SDE S_f of a probability density function $f(\theta)$ is defined as follows:

$$S_f = \int_{\theta \in \mathbb{R}} f(\theta) \ln f(\theta) d\theta, \quad \theta \in \mathbb{R} \tag{26}$$

2.4.1. Classifier features

Let $\hat{\mathbf{s}}_{k,i} = [\hat{\bar{x}}_{k,i} \ \hat{x}_{k,i} \ \hat{\dot{x}}_{k,i} \ \hat{\bar{y}}_{k,i} \ \hat{y}_{k,i} \ \hat{\dot{y}}_{k,i} \ \hat{\omega}_{k,i}]^T$ be the estimated state of ith point by UKS at time step k. Let $I_N = \{1, 2, \ldots, N\}$ and $I_S = \{i_s, i_s + 1,$

..., $i_s + N_s - 1\} \subset I_N$ be, respectively, the set of points on the endocardium, and endocardial wall of segment S, where N and N_S denote the corresponding number of points. This study uses fixed number of points over the cardiac cycles using subsampling the image space if needed, and therefore, I_N and I_S are constants. Similarly, we can define a new set of points, $\{\hat{s}'_{k,i}\}$, which corresponds to the endocardial boundary.

The center $(c_{x,k}, c_{y,k})$ of the endocardium at time step k is given by

$$c_x, k = \frac{1}{N}\sum_{i \in I_N}\hat{x}_{k,i}; \quad c_y, k = \frac{1}{N}\sum_{i \in I_N}\hat{y}_{k,i} \tag{27}$$

We propose to use the following classifier features (see Fig. 3 for an illustration).

2.4.1.1. Normalized radial distance. The normalized radial distance $r_{k,i}$ between the center $(c_{x,k}, c_{y,k})$ and a point $(x_{k,i}, y_{k,i})$ on the endocardial boundary is computed as follows:

$$r_{k,i} = \frac{\sqrt{(\hat{x}_{k,i} - c_x, k)^2 + (\hat{y}_{k,i} - c_y, k)^2}}{\max_{j \in I_S}\sqrt{(\hat{x}_{k,j} - c_{x,k})^2 + (\hat{y}_{k,j} - c_{y,k})^2}} \quad \forall i \in I_S \tag{28}$$

2.4.1.2. Radial velocity. We compute the radial velocity $v_{k,i}$ of an endocardial point $(x_{k,i}, y_{k,i})$ as follows:

$$v_{k,i} = \left\langle \vec{v}_{k,i} \cdot \frac{\vec{r}_{k,i}}{\|\vec{r}_{k,i}\|} \right\rangle \quad \forall i \in I_S \tag{29}$$

where $\vec{v}_{k,i} = [\hat{x}_{k,i}, \hat{y}_{k,i}]^T$ and $\vec{r}_{k,i} = [\hat{x}_{k,i} - c_{x,k}, \hat{y}_{k,i} - c_{y,k}]^T$

2.4.1.3. Segment arc length. An approximation of the arc length of an endocardial boundary described with a set of points, $\{(\hat{x}_{k,i}, \hat{y}_{k,i}) : i = i_s, \ldots, i_s + N_s - 1\}$, is computed as follows:

$$l_k = \sum_{i=i_s}^{i_s+N_s-2}\sqrt{(\hat{x}_{k,i+1} - \hat{x}_{k,i})^2 + (\hat{y}_{k,i+1} - \hat{y}_{k,i})^2} \tag{30}$$

In the above equation, the end index is equal to $i_s + N_s - 2$ since we start the computation with index $i + 1$.

2.4.1.4. Segment area. Let a_k denotes the area of the region enclosed within the endocardial boundary of segment S. We assume a_k corresponds to a convex polygon with vertices $\{(c_{x,k}, c_{y,k}), (\hat{x}_{k,i}, \hat{y}_{k,i}) : i = i_s, \ldots, i_s + N_s - 1\}$. The segment area is then computed as:

$$a_k = \frac{1}{2}\Big[\big(c_{x,k}\hat{y}_{k,i_s} - c_{y,k}\hat{x}_{k,i_s}\big) + \big(\hat{x}_{k,i_s+N_s-1}c_{y,k} - \hat{y}_{k,i_s+N_s-1}c_{x,k}\big)$$
$$+ \sum_{i=i_s}^{i_s+N_s-2}\big(\hat{x}_{k,i}\hat{y}_{k,i+1} - \hat{x}_{k,i+1}\hat{y}_{k,i}\big)\Big] \tag{31}$$

2.4.1.5. Wall thickness. The wall thickness of segment S is computed as follows:

$$\tau_k = \frac{2(a'_k - a_k)}{(l'_k + l_k)} \tag{32}$$

where a'_k is the area and l'_k the arc length of epicardial of segment S. The epicardial area a'_k and arc length l'_k can be computed similar to a_k and l_k using endocardial boundary points $\{\hat{s}'_{k,i}\}$.

2.4.2. Shannon's differential entropy and Bayesian classifier

We used all time points in computing the SDEs in this study. The kernel density estimate of a classifier element $\chi_n \in \{r_{k,i}, v_{k,i}, l_k, a_k, \tau_k\}$ for $k = 1, \ldots, K$ is given by

Table 1
Details of the datasets used in evaluation of the proposed method.

Description	Value
Number of subjects	58
Scanner protocol	FIESTA
Patient ages	16–79 years
Short-axis image resolution	(256×256) or (512×512) pixels
Number of frames (K)	20
Temporal resolution (ΔT)	29–76 ms
Pixel spacing	$(0.7 \times 0.7 \times 10.0)$–$(1.7 \times 1.7 \times 12.0)$ mm

$$f_{\chi_n}(\theta) = \frac{\sum_{n=1}^{n_\chi}\mathcal{K}(\chi_n - \theta)}{n_\chi} \quad \theta \in \mathbb{R} \tag{33}$$

where $n_\chi = KN_S$ for $\chi_n \in \{r_{k,i}, v_{k,i}\}$ and $n_\chi = K$ for $\chi_n \in \{l_k, a_k, \tau_k\}$. Typical choices of $\mathcal{K}(\cdot)$ are the Dirac function and the Gaussian kernel. Using the definition (26), the SDE is derived as follows:

$$S_{f_{\chi_n}}(\theta) = -\int_{\theta \in \mathbb{R}}$$
$$\times \frac{\sum \mathcal{K}(\chi_n - \theta)}{n_\chi}\Big(\ln\sum\mathcal{K}(\chi_n - \theta) - \ln n_\chi\Big)d\theta, \quad \theta$$
$$\in \mathbb{R} \tag{34}$$

It is advantageous to use multiple SDE measures towards the classification as they measure different information associated with the myocardial function. A naive Bayesian classifier (Seber, 1984) that provides a quadratic decision boundary is constructed from the SDEs of classifier features.

A naive Bayesian classifier (Seber, 1984) is constructed from the SDEs of classifier features, assuming that the features are independent. The Bayes classifier for a set of feature outcome $\{s_1, \ldots, s_n\}$ is defined as follows:

$$\text{classify } (s_1, \ldots, s_n) = \arg\max_c p(\mathbb{C} = c)\prod_{i=1}^{n}p(\mathbb{S}_i = s_i|\mathbb{C} = c) \tag{35}$$

where $\mathbb{S}_i$ denotes the ith classifier feature computed using (34), $\mathbb{C}$ denotes the set of classes $\{c\}$, $c = 1$ for normal and $c = 2$ for abnormal. $p(\mathbb{C} = c)$ denotes prior probability for class c, and $p(\mathbb{S}_i = s_i|\mathbb{C} = c)$ the likelihood of feature s_i given class c. $p(\mathbb{S}_i = s_i|\mathbb{C} = c)$ is assumed Gaussian with different variance values along $\mathbb{S}_i$-direction which yields a quadratic decision boundary.

3. Experiment and validation

The data contains 58×3 short-axis image datasets (i.e., apical, mid-cavity and basal), each consisting of 20 functional 2D images acquired from 21 normal and 37 abnormal hearts. The data were acquired on 1.5 T MRI scanners with fast imaging employing steady state acquisition (FIESTA) mode. The details of the datasets are presented in Table 1. The data consists of images from 41 male and 17 female subjects, and the average age of subjects is 52.3 ± 15.0 years. The temporal resolution (ΔT) is equal to 45.1 ± 8.8 ms. For each subject, three slices were respectively chosen from apical, mid-cavity and basal frames, and *anatomical landmarks* were identified manually on the first frame[2] (see Fig. 4 for an illustration). A cubic spline interpolation was used to sample $N = 120$ points along each endo- and epi-cardial boundary. The higher N, the better the estimation accuracy. However, the computational complexity of the algorithm increases with the values of N. The apical,

---

[2] As suggested by Cerqueira et al. (2002), the attachment of the right ventricular wall to the LV is used to identify and separate the septum from the LV anterior and inferior free walls.

mid-cavity and basal slices were automatically partitioned, respectively, into 4, 6 and 6 segments following the standard in (Cerqueira et al., 2002), which results in 16 segments per subject. The 17th segment, apex, was not analyzed. We used the registration algorithm in (Chen et al., 2010) to automatically propagate these segments in subsequent frames. The dynamic model and UKS parameters are chosen as $q_1 = 0.01$, $q_2 = 0.1$ $q_3 = 1$ and $r = 0.01$ to accommodate noise that accounts for modeling uncertainties. We used the Dirac function for $\mathcal{K}(\cdot)$ and 20 sample points (bins) in the kernel density estimation in (33).

The results of 928 myocardial segments (58 subjects × 16 segments) were compared with a single ground truth classification.[3] We classify a segment as abnormal if that segment is hypokinetic, akinetic or diskinetic. Among the 37 abnormal subjects, 12 were diagnosed with infarction, 10 with dilated cardiomyopathy and 15 with various heart diseases including resuscitated cardiac arrest, coronary artery occlusion, cardioembolic cerebrovascular accident and pseudo-aneurysm.

4. Results

In Fig. 5, we give a representative sample of the segmentation results for apical, mid-cavity and basal frames. We give the × and y position estimates of UKS plotted against the raw values obtained from the nonrigid registration for three representative sample points respectively from apical, mid-cavity and basal frames in Fig. 6. During the systolic phase, cardiac motion is at its peak, which causes higher uncertainties in motion estimation. Fig. 6 shows that estimation accuracy is higher at the beginning and end of the cardiac cycle, and lower in the middle. Fig. 7 shows the estimation of angular frequency ω_k using UKS for three representative sample points on apical, mid-cavity and basal frames. Note that the change in angular frequency at the end of the cardiac cycle in Fig. 7 could possibly be the result of the change in cardiac oscillation induced by cardiac muscles at the beginning of the systolic phase. We used two independent criteria to measure the performance of each classifier features, namely, the ROC curves (Zou et al., 2007) with corresponding AUCs (Hanley and McNeil, 1982), and Bhattacharyya measure (Comaniciu et al., 2003) to assess the discriminative power of each classifier features. Furthermore, we assessed the performance of the proposed approach via *leave-one-subject-out* method.

4.1. ROC, AUC and Bhattacharyya measure

The ROC curves for classifier features are shown in Fig. 8. We used same threshold for all segments and all slices. The ROC curves were obtained by varying such threshold. The figure shows that the SDEs of segment area and normalized radial distance have better classifying ability than other classifier features. The AUCs corresponding to the ROC curves in Fig. 8 are reported in Table 2. We used the Bhattacharyya distance metric to evaluate the overlap between the distributions of classifier features over normal and abnormal motions. The Bhattacharyya metric (Comaniciu et al., 2003) is given by

$$\mathcal{B} = \sqrt{1 - \sum_{y \in \mathbb{R}} \sqrt{f_N(y) f_A(y)}} \tag{36}$$

where f_N and f_A are the distributions over, respectively, normal and abnormal motions. The higher $\mathcal{B}$, the lesser the overlap (refer to Fig. 9 for an illustration) and, therefore, the better the discrimina-

Table 2
The area under the curve corresponding to Fig. 8 and the Bhattacharyya distance metric ($\mathcal{B}$) of normal/abnormal distributions. The higher the values the better the discriminative ability of the classifier.

Classifier element	AUC (%)	Bhattacharyya distance metric ($\mathcal{B}$)
The SDE of:		
Normalized radial distance	91.6	0.60
Segment area	90.5	0.59
Wall thickness	86.6	0.49
Segment arc length	85.7	0.48
Radial velocity	80.0	0.38

Table 3
Classification accuracy of the proposed method among different cardiovascular diseases.

Disease	Classification accuracy (%)
Infarction	79.7
Dilated cardiomyopathy	87.5
Other cardiovascular diseases	82.9

tive ability of the classifier. The SDEs of segment area and normalized radial distance yielded the higher $\mathcal{B}$ as reported in Table 2 and, therefore, have the best discriminative ability. This is consistent with the evaluations based on ROC/AUC.

4.2. Classification performance

A naive Bayes classifier algorithm is constructed from the SDEs of the segment area and normalized radial distance, the features with better classifier ability. Fig. 10 shows the quadratic decision boundary for normal/abnormal classification with the proposed method (with the UKS), where blue circles represent the normal function and red triangles the abnormal. These boundaries were constructed separately for apical, mid-cavity and basal frames, following a learning from all 58 subjects.

The evaluations of classification performance in terms of accuracy, sensitivity and specificity are given by

$$\text{accuracy} = \frac{T_P + T_N}{P + N}, \quad \text{specificity} = \frac{T_N}{N}, \quad \text{sensitivity} = \frac{T_P}{P} \tag{37}$$

where T_P is true positives (number of segments correctly classified as "*Abnormal*") and T_N true negatives (number of segments correctly classified as "*Normal*"). The total number of "*Abnormal*" and "*Normal*" segments are P and N, respectively. Table 4 compares the classification performance of correctly classified hearts with the proposed method with and without the UKS, using a *leaving-one-subject-out*[4] method. The overall classification accuracy for the proposed method with UKS is equal to 87.1%, with a sensitivity of 86.8% and specificity of 87.2%. The method without temporal smoothing yielded a lower overall classification accuracy of 84.7%, with a sensitivity of 84.8% and Specificity of 84.6%. The results show that UKS enhances significantly the accuracy of classification. The highest performance of the proposed method was achieved for mid-cavity frames, with an average accuracy of 89.4%, a sensitivity of 87.8% and a specificity of 90.3%. The accuracy of correct classification among different heart diseases are given in Table 3.

Table 5 reports comparisons of the obtained results to visual scores by experienced radiologists. We computed the Kappa statistics (Viera and Garret, 2005) between the proposed method and

Table 4
Comparison of the percentage of classification accuracy using leaving-one-subject-out method for the proposed method with UKS and without temporal smoothing. The proposed method with UKS achieved an overall classification accuracy of 87.1%, whereas the method without temporal smoothing achieved 88.3%.

	The proposed method (with UKS)			Without UKS		
	Accuracy (%)	Sensitivity (%)	Specificity (%)	Accuracy (%)	Sensitivity (%)	Specificity (%)
Apex	84.5	85.3	83.8	82.8	84.3	81.5
Mid-cavity	89.4	87.8	90.3	87.1	84.0	88.9
Base	86.5	87.1	86.2	83.6	86.2	82.3
Overall	**87.1**	**86.8**	**87.2**	**84.7**	**84.8**	**84.6**

Table 5
Comparisons between the proposed method and visual wall motion scoring by experienced radiologists in detecting regional wall motion abnormality. The proposed method yielded a kappa measure of 0.73, a *substantial agreement* with radiologists' results.

	Visual wall motion scoring		
	Abnormal	Normal	Total
The proposed method			
Abnormal	**303**	74	377
Normal	46	**505**	551
Total	349	579	928

radiologists' findings as follows. The observed percentage agreement is:

$$p(a) = \frac{303 + 505}{928} = 0.87 \tag{38}$$

The overall probability of random agreement is:

$$p(e) = \frac{349}{928} \cdot \frac{377}{928} + \frac{579}{928} \cdot \frac{551}{928} = 0.52 \tag{39}$$

Therefore, the Cohen's kappa is:

$$\kappa = \frac{p(a) - p(e)}{1 - p(e)} = 0.73 \tag{40}$$

a value which indicates a substantial agreement (Viera and Garret, 2005) between the proposed method and visual scoring. The kappa measure between the method without UKS and visual wall motion scoring was 0.68.

A representative example of classification by the proposed method and corresponding ground truth classification by radiologists are given in Fig. 11. The normal and abnormal motions are depicted by, respectively, green and red regions. Comparisons with ground truth classifications show that 15 out of 16 segments were correctly classified by the proposed method in this example.

5. Conclusions

In this study, we investigate the problem of detecting and localizing myocardial abnormal motion automatically. We proposed a nonlinear state transition model to characterize myocardial motion and the unscented Kalman smoother for state estimation. We also proposed to use a nonrigid registration method to obtain sequence of points over time, given initial segmentation on the first frame. We followed the standard issued by American Heart Association to identify the myocardial segments, and the results were analyzed using information theoretic measures based on Shannon's differential entropy (SDE). The SDE of normalized radial distance, radial velocity, segment area, segment arc length and wall thickness were evaluated for each myocardial segment, and a naive Bayesian classifier is constructed from the SDEs. The experimental analysis carried over apical, mid-cavity and basal sequences, each consisting of 20 frames of short-axis MR images obtained from 58 subjects demonstrates that the proposed method

performs significantly better than other recent methods, and can lead to a promising diagnostic support tool to assists clinicians.

6. Limitations of the proposed study

The following lists the limitations of the proposed study.

- Although all frames contribute to the SDEs for each classifier feature, the method uses density functions of classifier elements and, therefore, it does not include the temporal characteristics in classification.
- The algorithm requires a user input on the first frame to identify the endo- and epicardial boundaries as well as the septal wall.
- Although our ground truth was built by three radiologists, it is still considered a single ground truth because each radiologist annotated a different portion of the data set.

Appendix A. Derivation of discrete dynamic model

Let us consider the *continuous state-space* model (12).

$$\dot{\zeta}(t) = \begin{bmatrix} 0 & 0 & 0 \\ 0 & 0 & 1 \\ \omega^2 & -\omega^2 & 0 \end{bmatrix} \zeta(t) + \begin{bmatrix} 1 & 0 \\ 0 & 0 \\ 0 & 1 \end{bmatrix} w(t) = A(\omega)\zeta(t) + Bw(t) \tag{A.1}$$

The continuous-time state Eq. (A.1) has the following solution:

$$\zeta(t) = F(t, t_0)\zeta(t_0) + \int_{t_0}^{t} F(t, \tau)Bw(\tau)d\tau \tag{A.2}$$

The transition matrix has the following properties:

$$\frac{dF(t, t_0)}{dt} = A(t)F(t, t_0) \tag{A.3}$$

$$F(t_2, t_0) = F(t_2, t_1)F(t_1, t_0) \quad \forall t_1 \tag{A.4}$$

$$F(t, t) = I \tag{A.5}$$

From (A.4) and (A.5), we obtain

$$F(t, t_0) = F(t_0, t)^{-1} \tag{A.6}$$

The transition matrix has no explicit form unless it satisfies the following *commutative property*.

$$A(t) \int_{t_0}^{t} A(\tau)d\tau = \int_{t_0}^{t} A(\tau)d\tau A(t) \tag{A.7}$$

Then,

$$F(t, t_0) = \exp\left(\int_{t_0}^{t} A(\tau)d\tau \right) \tag{A.8}$$

For a time-invariant system, assuming $t_0 = 0$

$$F(t) \triangleq F(t, 0) = \exp(At) \tag{A.9}$$

The transition matrix A of the continuous state-space model (A.1) is given by

$$A = \begin{bmatrix} 0 & 0 & 0 \\ 0 & 0 & 1 \\ \omega^2 & -\omega^2 & 0 \end{bmatrix} \tag{A.10}$$

Evaluating exp (At) yields

$$\exp(At) = \begin{bmatrix} 1 & 0 & 0 \\ 1-\cos(\omega t) & \cos(\omega t) & \frac{1}{\omega}\sin(\omega t) \\ \omega\sin(\omega t) & -\omega\sin(\omega t) & \cos(\omega t) \end{bmatrix} \tag{A.11}$$

The state at sampling time t_{k+1} can be written as

$$\zeta(t_{k+1}) = F(t_{k+1}, t_k)\zeta(t_k) + w(t_k) \tag{A.12}$$

For a *time-invariant* continuous-time system, the transition matrix is

$$F(t_{k+1}, t_k) = F(t_{k+1} - t_k) = \exp((t_{k+1} - t_k)A) \triangleq F_k \tag{A.13}$$

The discrete-time process noise relates to that of continuous-time as follows

$$w(t_k) = \int_{t_k}^{t_{k+1}} \exp((t_{k+1} - \tau)A)Bw(\tau)d\tau \triangleq w(k) \tag{A.14}$$

We assume $w(t)$ is zero-mean and white noise. It follows that

$$\mathbb{E}[w(k)] = \mathbf{0}_{2\times 1} \tag{A.15}$$

$$\mathbb{E}[w(k)w(l)^T] = Q_k \delta_{kl} \tag{A.16}$$

where δ_{kl} is the Kronecker delta function. The covariance Q_k can be simplified as

$$Q_k = \int_{t_k}^{t_{k+1}} \exp((t_{k+1} - \tau)A)B\Gamma(\tau)B^T\exp((t_{k+1} - \tau)A^T)d\tau \tag{A.17}$$

where

$$\Gamma(\tau) = \mathbb{E}[w(\tau)w(\tau)^T] \tag{A.18}$$

$$= \begin{bmatrix} q_1^2 & 0 \\ 0 & q_2^2 \end{bmatrix} \tag{A.19}$$

Parameters q_1 and q_2, and q_3 (recall that q_3 is the third diagonal element of the process covariance matrix) characterize, respectively, the uncertainties associated with the mean position, velocity and angular frequency elements of the state vector. On the one hand, smaller values of q_1, q_2 and q_3 enforces the conformity of LV motion to the model, thereby affecting the accuracy of the results when the motion deviates from the model. On the other hand, larger values of q_1, q_2 and q_3 allow higher uncertainties within the model, which may result in poor temporal consistency.

Solving (A.17) yields

$$Q_k = [q_{ij}]_{3\times 3} \tag{A.20}$$

where

$$q_{11} = q_1^2 \Delta T \tag{A.21}$$

$$q_{12} = q_{21} = \frac{q_1^2(\omega\Delta T - \sin(\omega\Delta T))}{\omega} \tag{A.22}$$

$$q_{13} = q_{31} = q_1^2(1 - \cos(\omega\Delta T)) \tag{A.23}$$

$$q_{22} = \frac{q_1^2\omega^2(3\omega\Delta T - 4\sin(\omega\Delta T) + \cos(\omega\Delta T)\sin(\omega\Delta T)) + q_2^2(\omega\Delta T - \cos(\omega\Delta T)\sin(\omega\Delta T))}{2\omega^3} \tag{A.24}$$

$$q_{23} = q_{32}$$
$$= \frac{q_1^2\omega^2(1 - 2\cos(\omega\Delta T) + \cos^2(\omega\Delta T)) + q_2^2\sin^2(\omega\Delta T)}{2\omega^2} \tag{A.25}$$

$$q_{33} = -\frac{q_1^2\omega^2(\cos(\omega\Delta T)\sin(\omega\Delta T) - \omega\Delta T) - q_2^2(\cos(\omega\Delta T)\sin(\omega\Delta T) - \omega\Delta T)}{2\omega} \tag{A.26}$$

Appendix B. Unscented Kalman smoother

Consider the state transition Eq. (16) and the corresponding measurement Eq. (18).

$$\mathbf{s}_{k+1} = f_k(\mathbf{s}_k) + v_k \tag{B.1}$$

$$z_k = H_k\mathbf{s}_k + \eta_k \tag{B.2}$$

Our objective is to compute a Gaussian approximation to the smoothing distribution $p(\mathbf{s}_k|z_{1:K}) \approx \mathcal{N}(\mathbf{s}_k|m_k^s, P_k^s)$, where m_k^s and P_k^s are the mean and covariance of the state $\mathbf{s}_k$, and $z_{1:K} = \{z_1, z_2, \ldots, z_K\}$. First, we consider the prediction and update distribution of the *optimal filtering equations* corresponding the state-space model given by (B.1) and (B.2).

1. Prediction:

$$p(\mathbf{s}_k|z_{1:k-1}) = \int p(\mathbf{s}_k|\mathbf{s}_{k-1})p(\mathbf{s}_{k-1}|z_{1:k-1}) \, d\mathbf{s}_{k-1} \tag{B.3}$$

2. update:

$$p(\mathbf{s}_k|z_{1:k}) = \frac{p(z_k|\mathbf{s}_k)p(\mathbf{s}_k|z_{1:k-1})}{\int p(z_k|\mathbf{s}_k)p(\mathbf{s}_k|z_{1:k-1}) \, d\mathbf{s}_k} \tag{B.4}$$

The *optimal smoothing equations* corresponding to forward–backward smoother can be written as follows:

$$p(\mathbf{s}_k|z_{1:K}) = p(\mathbf{s}_k|z_{1:k}) \int \frac{p(\mathbf{s}_{k+1}|\mathbf{s}_k)p(\mathbf{s}_{k+1}|z_{1:K})}{p(\mathbf{s}_{k+1}|z_{1:k})} \, d\mathbf{s}_{k+1} \tag{B.5}$$

These optimal filtering and smoothing distributions are computationally intractable and, therefore, numerical approximations are required. We can use the *unscented Rauch-Tung-Striebel (RTS) smoother* to find the approximate smoothing distributions.

The smoothing update Eq. (B.4) can be divided into the following three steps.

1. Form the joint distribution of $\mathbf{s}_k$ and $\mathbf{s}_{k+1}$, given $z_{1:k}$.

$$p(\mathbf{s}_k, \mathbf{s}_{k+1}|z_{1:k}) = p(\mathbf{s}_{k+1}|\mathbf{s}_k)p(\mathbf{s}_k|z_{1:k}) \tag{B.6}$$

2. Compute the conditional distribution

$$p(\mathbf{s}_k|\mathbf{s}_{k+1}, z_{1:k}) = \frac{p(\mathbf{s}_k, \mathbf{s}_{k+1}|z_{1:k})}{p(\mathbf{s}_{k+1}|z_{1:k})} \tag{B.7}$$

where the denominator term is given by

$$p(\mathbf{s}_{k+1}|z_{1:k}) = \int p(\mathbf{s}_{k+1}|\mathbf{s}_k)p(\mathbf{s}_k|z_{1:k}) \, d\mathbf{s}_k \tag{B.8}$$

Applying Markov property of the state-space model, we have $p(\mathbf{s}_k|\mathbf{s}_{k+1}, z_{1:K}) = p(\mathbf{s}_k|\mathbf{s}_{k+1}, z_{1:k})$. Thus,

$$p(\mathbf{s}_k|\mathbf{s}_{k+1}, z_{1:K}) = \frac{p(\mathbf{s}_k, \mathbf{s}_{k+1}|z_{1:k})}{p(\mathbf{s}_{k+1}|z_{1:k})} \tag{B.9}$$

3. Compute the joint distribution of $\mathbf{s}_k$ and $\mathbf{s}_{k+1}$, given $z_{1:K}$

$$p(\mathbf{s}_k, \mathbf{s}_{k+1}|z_{1:K}) = p(\mathbf{s}_k|\mathbf{s}_{k+1}, z_{1:K})p(\mathbf{s}_{k+1}z_{1:K}) \, d\mathbf{s}_{k+1} \tag{B.10}$$

Now, the smoothing distribution of $\mathbf{s}_k$ is given by marginalizing the joint distribution over $\mathbf{s}_{k+1}$:

$$p(\mathbf{s}_k|z_{1:K}) = \int p(\mathbf{s}_k|\mathbf{s}_{k+1}, z_{1:K})p(\mathbf{s}_{k+1}|z_{1:K}) \, d\mathbf{s}_{k+1} \tag{B.11}$$

Here, we assume that the mean m_k and covariance P_k of the distribution $p(\mathbf{s}_k|z_{1:k}) \approx \mathcal{N}(\mathbf{s}_k|m_k, P_k)$ for the state-space given by (B.1) and (B.2) have been computed by the UKF. We also assume that the smoothing distribution $p(\mathbf{s}_{k+1}|z_{1:K}) \approx \mathcal{N}(\mathbf{s}_{k+1}|m_{k+1}^s, P_{k+1}^s)$ of time step $k + 1$ is known and Gaussian. We can derive an approximation to the optimal smoothing based on unscented transform as follows:

1. Compute the unscented transformation based Gaussian approximation to the joint distribution $p(\mathbf{s}_k, \mathbf{s}_{k+1}|z_{1:k})$ in (B.6).

$$\begin{bmatrix} \mathbf{s}_k \\ \mathbf{s}_{k+1} \end{bmatrix}\Big|z_{1:k} \sim \mathcal{N}\left(\begin{bmatrix} m_k \\ m_{k+1} \end{bmatrix}, \begin{bmatrix} P_k & C_{k+1} \\ C_{k+1} & P_{k+1} \end{bmatrix}\right) \tag{B.12}$$

This is done by augmenting the process noise v_k with the state $\mathbf{s}_k$ to form a new state variable $\tilde{\mathbf{s}}_k = [\mathbf{s}_k \ v_k]^T$, which then has the distribution

$$\tilde{\mathbf{s}}_k|z_{1:k} \sim \mathcal{N}\left(\begin{bmatrix} m_k \\ 0 \end{bmatrix}, \begin{bmatrix} P_k & 0 \\ 0 & Q_k \end{bmatrix}\right) \tag{B.13}$$

2. Now, we can compute the approximate distributions for (B.7) and (B.9), using (B.12) and computation rules of Gaussian distributions. This results in

$$\mathbf{s}_k|z_{1:K} \sim \mathcal{N}(m_{k+1}', P_{k+1}') \tag{B.14}$$

where

$$D_k = C_{k+1}[P_{k+1}^-]^{-1} \tag{B.15}$$
$$m_{k+1}' = m_k + D_k(\mathbf{s}_{k+1} - m_{k+1}^-) \tag{B.16}$$
$$P_{k+1}' = P_k - D_k P_{k+1}^- D_k^T \tag{B.17}$$

3. Now, we can compute the approximate distribution of $p(\mathbf{s}_k, \mathbf{s}_{k+1}|z_{1:K})$ in (B.10).

$$\begin{bmatrix} \mathbf{s}_k \\ \mathbf{s}_{k+1} \end{bmatrix}\Big|z_{1:K} \sim \mathcal{N}(m_{k+1}'', P_{k+1}'') \tag{B.18}$$

where

$$m_{k+1}'' = \begin{bmatrix} m_k + D_k(\mathbf{s}_{k+1} - m_{k+1}^-) \\ m_{k+1}^s \end{bmatrix} \tag{B.19}$$

$$P_{k+1}'' = \begin{bmatrix} D_k P_{k+1}^s D_k^T + P_{k+1}' & D_k P_{k+1}^s \\ P_{k+1}^s D^T & P_{k+1}^s \end{bmatrix} \tag{B.20}$$

Finally, we can compute the Gaussian approximation to the smoothing distribution at time step k:

$$\mathbf{s}_k|z_{1:k} \sim \mathcal{N}(m_{k+1}^s, P_{k+1}^s) \tag{B.21}$$

where

$$m_k^s = m_k + D_k[m_{k+1}^s - m_{k+1}^-] \tag{B.22}$$
$$P_k^s = P_k + D_k[P_{k+1}^s - P_{k+1}]D_k^T \tag{B.23}$$

Appendix C. Supplementary material

Supplementary data associated with this article can be found, in the online version, at http://dx.doi.org/10.1016/j.media.2012.11.007.

References

Ben Ayed, I., Li, S., Ross, I., 2009. Embedding overlap priors in variational left ventricle tracking. IEEE Transactions on Medical Imaging 28, 1902–1913.

Ben Ayed, I., Lu, Y., Li, S., Ross, I., 2008. Left ventricle tracking using overlap priors. In: Metaxas, D. et al. (Eds.), MICCAI 2008. Springer, pp. 1025–1033.

Bergvall, E., Hedstrom, E., Bloch, K., Arheden, H., Sparr, G., 2008. Spline-based cardiac motion tracking using velocity-encoded magnetic resonance imaging. IEEE Transactions on Medical Imaging 27, 1045–1053.

Bosch, J.G., Nijland, F., Mitchell, S.C., Lelieveldt, B.P., Kamp, O., Reiber, J.H., Sonka, M., 2005. Computer-aided diagnosis via model-based shape analysis: automated classification of wall motion abnormalities in echocardiograms. Academic Radiology 12, 358–367.

Cerqueira, M.D., Weissman, N.J., Dilsizian, V., Jacobs, A.K., Kaul, S., Laskey, W.K., Pennell, D.J., Rumberger, J.A., Ryan, T., Verani, M.S., 2002. Standardized myocardial segmentation and nomenclature for tomographic imaging of the heart: a statement for healthcare professionals from the cardiac imaging committee of the council on clinical cardiology of the American Heart Association. Circulation 105, 539–542.

Chen, H.m., Goela, A., Garvin, G.J., Li, S., 2010. A parameterization of deformation fields for diffeomorphic image registration and its application to myocardial delineation. In: Jiang, T. et al. (Eds.), MICCAI 2010. Springer, pp. 340–348.

Comaniciu, D., Ramesh, V., Meer, P., 2003. Kernel-based object tracking. IEEE Transactions on Pattern Analysis and Machine Intelligence 25, 564–577.

Fung, G., Qazi, M., Krishnan, S., Bi, J., Rao, B., Katz, A., 2005. Sparse classifiers for automated heartwall motion abnormality detection. In: Proc. IEEE 4th Int. Conf. Machine Learning and Applications, pp. 194–200.

Garcia-Barnes, J., Gil, D., Badiella, L., Hernandez-Sabate, A., Carreras, F., Pujades, S., Marti, E., 2010. A normalized framework for the design of feature spaces assessing the left ventricular function. IEEE Transactions on Medical Imaging 29, 733–745.

Gilliam, A., Epstein, F., Acton, S., 2009. Cardiac motion recovery via active trajectory field models. IEEE Transactions on Information Technology in Biomedicine 13, 226–235.

Hanley, J., McNeil, B., 1982. The meaning and use of the area under a receiver operating characteristic (ROC) curve. Radiology 143, 29–36.

Hoffmann, R., von Bardeleben, S., Kasprzak, J.D., Borges, A.C., ten Cate, F., Firschke, C., Lafitte, S., Al-Saadi, N., Kuntz-Hehner, S., Horstick, G., Greis, C., Engelhardt, M., Vanoverschelde, J.L., Becher, H., 2006. Analysis of regional left ventricular function by cineventriculography, cardiac magnetic resonance imaging, and unenhanced and contrast-enhanced echocardiography: a multicenter comparison of methods. Journal of the American College of Cardiology 47, 121–128.

Jacob, G., Noble, J.A., Kelion, A.D., Banning, A.P., 2001. Quantitative regional analysis of myocardial wall motion. Ultrasound in Medicine & Biology 27, 773–784.

Julier, S., Uhlmann, J., 2004. Unscented filtering and nonlinear estimation. Proceedings of the IEEE 92, 401–422.

Lekadir, K., Keenan, N., Pennell, D., Yang, G., 2011. An inter-landmark approach to 4-d shape extraction and interpretation: application to myocardial motion assessment in MRI. IEEE Transactions on Medical Imaging 30, 52–68.

Leung, K.Y., Bosch, J.G., 2007. Localized shape variations for classifying wall motion in echocardiograms. In: Ayache, N. et al. (Eds.), MICCAI 2007. Springer-Verlag, Berlin, Heidelberg, pp. 52–59.

Liu, H., Shi, P., 2007. State-space analysis of cardiac motion with biomechanical constraints. IEEE Transactions on Image Processing 16, 901–917.

Liu, J., 2006. New Development of the Deformation Method. Ph.D. thesis, Department of Mathematics, The University of Texas at Arlington.

Liu, X., Prince, J.L., 2010. Shortest path refinement for motion estimation from tagged MR images. IEEE Transactions on Medical Imaging 29, 1560–1572.

Lu, Y., Radau, P., Connelly, K., Dick, A., Wright, G., 2009. Pattern recognition of abnormal left ventricle wall motion in cardiac MR. In: Yang, G.Z. et al. (Eds.), MICCAI 2009. Springer, pp. 750–758.

Mansor, S., Noble, J., 2008. Local wall motion classification of stress echocardiography using a hidden Markov model approach. In: The 5th IEEE Int. Symp. Biomedical Imaging: From Nano to Macro, pp. 1295–1298.

Moireau, P., Chapelle, D., Tallec, P.L., 2009. Filtering for distributed mechanical systems using position measurements: perspectives in medical imaging. Inverse Problems 25, 035010.

Pan, L., Prince, J., Lima, J., Osman, N., 2005. Fast tracking of cardiac motion using 3D-HARP. IEEE Transactions on Biomedical Engineering 52, 1425–1435.

Petitjean, C., Dacher, J.N., 2011. A review of segmentation methods in short axis cardiac MR images. Medical Image Analysis 15, 169–184.

Punithakumar, K., Ben Ayed, I., Islam, A., Ross, I.G., Li, S., 2010a. Regional heart motion abnormality detection via information measures and unscented Kalman filtering. In: Jiang, T. et al. (Eds.), MICCAI 2010. Springer, pp. 409–417.

Punithakumar, K., Ben Ayed, I., Islam, A., Ross, I.G., Li, S., 2010b. Tracking endocardial motion via multiple model filtering. IEEE Transactions on Biomedical Engineering 57, 2001–2010.

Punithakumar, K., Ben Ayed, I., Ross, I.G., Islam, A., Chong, J., Li, S., 2010c. Detection of left ventricular motion abnormality via information measures and bayesian filtering. IEEE Transactions on Information Technology in Biomedicine 14, 1106–1113.

Qazi, M., Fung, G., Krishnan, S., Bi, J., Bharat Rao, R., Katz, A., 2007. Automated heart abnormality detection using sparse linear classifiers. IEEE Engineering in Medicine and Biology Magazine 26, 56–63.

Qian, Z., Liu, Q., Metaxas, D.N., Axel, L., 2008. Identifying regional cardiac abnormalities from myocardial strains using spatio-temporal tensor analysis. In: Metaxas, D. et al. (Eds.), MICCAI 2008. Springer, pp. 789–797.

Arts, T., Prinzen, F., Delhaas, T., Milles, J., Rossi, A., Clarysse, P., 2010. Mapping displacement and deformation of the heart with local sine-wave modeling. IEEE Transactions on Medical Imaging 29, 1114–1123.

Bar-Shalom, Y., Kirubarajan, T., Li, X.R., 2002. Estimation with Applications to Tracking and Navigation. John Wiley & Sons Inc., New York, NY, USA.

Redheuil, A.B., Kachenoura, N., Laporte, R., Azarine, A., Lyon, X., Jolivet, O., Frouin, F., Mousseaux, E., 2007. Interobserver variability in assessing segmental function can be reduced by combining visual analysis of cmr cine sequences with corresponding parametric images of myocardial contraction. Journal of Cardiovascular Magnetic Resonance 9, 863–872.

Sarkka, S., 2008. Unscented Rauch–Tung–Striebel smoother. IEEE Transactions on Automatic Control 53, 845–849.

Seber, G.A.F., 1984. Multivariate Observations. John Wiley & Sons Inc., Hoboken, NJ.

Spottiswoode, B., Zhong, X., Hess, A., Kramer, C., Meintjes, E., Mayosi, B., Epstein, F., 2007. Tracking myocardial motion from cine dense images using spatiotemporal phase unwrapping and temporal fitting. IEEE Transactions on Medical Imaging 26, 15–30.

Suinesiaputra, A., Frangi, A., Kaandorp, T., Lamb, H., Bax, J., Reiber, J., Lelieveldt, B., 2009. Automated detection of regional wall motion abnormalities based on a statistical model applied to multislice short-axis cardiac MR images. IEEE Transactions on Medical Imaging 28, 595–607.

Viera, A.J., Garret, J.M., 2005. Understanding interobserver agreement: the kappa statistic. Family Medicine 37, 360–363.

Young, A.A., 1999. Model tags: direct three-dimensional tracking of heart wall motion from tagged magnetic resonance images. Medical Image Analysis 3, 361–372.

Zhou, X., 2006. On uniqueness theorem of a vector function. Progress in Electromagnetics Research 65, 93–102.

Zou, K.H., O'Malley, J.A., Mauri, L., 2007. Receiver-operating characteristic analysis for evaluating diagnostic tests and predictive models. Circulation 115, 654–657.